Structure-property orientation relationship of a $\gamma/\alpha_2/Ti_5Si_3$ in as-cast Ti-45Al-2Nb-0.7Cr-0.3Si intermetallic alloy

M.N. Mathabathe, A.S. Bolokang, G. Govender, R.J. Mostert, C.W. Siyasiya

PII: S0925-8388(18)32386-7

DOI: 10.1016/j.jallcom.2018.06.265

Reference: JALCOM 46601

To appear in: *Journal of Alloys and Compounds*

Received Date: 16 May 2018

Revised Date: 20 June 2018

Accepted Date: 22 June 2018

Please cite this article as: M.N. Mathabathe, A.S. Bolokang, G. Govender, R.J. Mostert, C.W. Siyasiya, Structure-property orientation relationship of a $\gamma/\alpha_2/Ti_5Si_3$ in as-cast Ti-45Al-2Nb-0.7Cr-0.3Si intermetallic alloy, *Journal of Alloys and Compounds* (2018), doi: 10.1016/j.jallcom.2018.06.265.

Structure-property orientation relationship of a $\gamma/\alpha_2/Ti_5Si_3$ in as-cast Ti-45Al-2Nb-0.7Cr-0.3Si intermetallic alloy

M. N. Mathabathe[a,b*], A. S. Bolokang[b**], G. Govender[b], R.J. Mostert[a], C.W. Siyasiya[a]

[a]Department of Material Science and Metallurgical Engineering, Faculty of Engineering, Built Environment and Information Technology, University of Pretoria, South Africa

[b]Council of Scientific Industrial Research, Materials Science and Manufacturing, Light Metals, Meiring Naude Road, P O Box 395 Pretoria, South Africa

Abstract

Structure-property relationship of the as-cast γ-Ti-45Al-2Nb-0.7Cr-0.3Si based intermetallic alloy was examined. The phases stable at room temperature in the alloy were $\gamma/\alpha_2/Ti_5Si_3$, respectively; while their crystal structures were described by means of chemical formulas, Pearson's number, space groups, lattice parameters, atomic positions and occupancy numbers using a Vienna *ab* initio simulation package (VASP) software for materials design. Moreover, high resolution electron backscatter diffraction (HSEBSD) was used to analyse the orientation relationship of both the as-cast (β-solidifying) and heat-treated (α-solidifying) microstructural phases. The results showed that the formation of $\gamma/\alpha_2/Ti_5Si_3$ follows the Blackburn orientation relationship (BOR): (β-solidifying) $\{110\}^{\beta} // \{0001\}^{\alpha}$ and $<111>^{\beta} // <2\bar{1}\bar{1}0>^{\alpha}$, and for (α-solidifying) = $(111)\gamma \,||\, (0001)\alpha$ and $<1\bar{1}0]\gamma \,||\, <11\bar{2}0>\alpha$.

Keywords: Crystal structures; $\gamma/\alpha_2/Ti_5Si_3$; Intermetallic; Blackburn orientation relationship

*Corresponding Author: Maria.N. Mathabathe, Tel: (+27) 12 841 7224

Email: nmathabathe@csir.co.za

**Corresponding Author: Amogelang S. Bolokang, Tel: (+27) 12 841 3295,

Email: sbolokang@csir.co.za

1. Introduction

Gamma-Titanium aluminide (γ-TiAl) intermetallic compound with an ordered $L1_0$ (space group P4/mmm, prototype CuAu) crystal structure, represent an important class of structural materials with excellent physical and mechanical properties, potential for aerospace and automotive industries applications. In particular for engineering applications where weight reduction, improved fuel consumption and high temperature efficiency are of essential requirement **[1-3]**. However, functional applications of TiAl alloys are hindered by its lack of room temperature ductility and fracture toughness. In order to overcome these drawbacks, micro-alloying with ternary elements is implemented. Intrinsic ductility of TiAl is due to directional Al p and Ti d covalent bonds, as a result ternary additions that can weaken the p-d interactions may effectively enhance the ductility of TiAl **[4]**. Furthermore, alloying elements that can lower the axial *c/a* ratio of TiAl close to unity may lead to an increase in the number of deformation modes, and consequently with improved ductility **[4]**. However, alloying with strong beta-stabilising elements such as (Cr, Nb, W and Mo) refine the grain structure and improve high temperature deformation ability as a result of stabilised metastable B2 phase (ordered phase of β at low temperature) **[5,6]**. However, small additions of silicon enhances high temperature oxidation resistance, in particular the fine coherent Ti_5Si_3 particles formed during eutectoid reaction along lamellar interfaces intensifies creep resistance **[7]**. The presence of coarse Ti_5Si_3 particles in the microstructure suggest that the particles may have precipitated directly from the liquid that consequently reduces tensile properties **[7]**. Phase transformations and evolution of lamellar structure in Ti-Al alloys is of great interest **[8-11]**. Moreover, other investigations validated that a fine grained fully lamellar structure (FFLS) exhibit a balance of mechanical properties **[12]**. Various methods have been used to obtain a FFLS in previous studies. Jin et al., **[12]** reported two thermomechanical mechanism of achieving the structure. The first method involves forging or extrusion at a temperature lower than the α transus temperature ($T\alpha$), heat-treated at $T \geq T\alpha$ and/or directly extruding the alloy at $T \geq T\alpha$. The second technique involves conversion of a coarse grained structure (originated from α-solidification) into a FFLS by cyclic heat-treatment. The refinement of lamellar structure was achieved by the combination of the refinement of Al-supersaturated α_2-Ti_3Al grains and the introduction of dislocations prior to aging **[13]**. The lamellar coarsening process is influenced by the lamellar shrinkage and termination annihilation as well as by the merging of lamellae **[14, 15]**. The lamellar structure is also of interest in other class of materials in engineering and biomedical applications **[16-18]**. In order to gain fundamental understanding of the role of alloying elements in modifying the structural, electronic and mechanical properties of TiAl, specific knowledge of the lattice site occupancy behaviour is crucial. The current investigation aim to present an undivided picture of the T= 0 K site preference of alloying elements in TiAl using first-principle calculations to thermodynamically model the developing γ-Ti-45Al-2Nb-0.7Cr-0.3Si microstructure. It is of paramount importance to acquire knowledge of why, how, and what collective effect on the $\gamma/\alpha_2/Ti_5Si_3$ have on the arc button melted and heat-treated γ-TiAl based intermetallic alloy.

2. Experimental procedure

2.1 First principle calculations

The commonly known computational technique is the *ab initio* method (employed in this study), also known as the Vienna ab Initio simulation package (VASP) which is a group of methods which enables the determination of properties of materials viz. the fundamental constants and atomic positions. Therefore, first principle calculations are preformed using projector augmented wave (PAW) pseudopotentials within the generalised gradient approximation (PW91-GGA), AS implemented in the (VASP) **[19]**. An energy cut-off of 500 eV was used, as it was sufficient to converge the total energy of the TiAl alloys. For the exchange-correlation functional, the generalized gradient approximation of Perdew and Wang (GGA-PBE) **[20]** was chosen. The Brillouin zone integrations were performed for suitably large sets of k-points according to Monkhorst and Pack Pack **[21]**. The phonon dispersion spectra were evaluated using PHONON code **[22]** as implemented by Materials Design within their MedeA software, VASP code. All the calculations were done at 0 K. Kang et al. **[23],** reported that for doped (alloyed) systems, geometry optimisation is performed to obtain a stable structure with minimum total energy. In addition, the geometry optimization process was performed on all atomic positions that were relaxed, until forces are less than 0.05 eV/Ǻ and stresses less than 0.1 GPa. However, in the present study, the geometry optimisation for the Ti-Al-X$_{(Nb,\ Cr,\ Si)}$ based alloys were performed within generalised gradient approximation using the energy cut-off of 500eV, and the lattice parameters allowed to vary.

2.2 Mechanical properties

The calculated elastic constants allow us to obtain the macroscopic mechanical parameters of all systems e.g. bulk modulus *K*, shear modulus *G* and elastic modulus *E*. However, for all crystal structures, *K*, *G* and *E* of polycrystalline materials are predicted by the following Voight equations **[23]:**

$$K = \frac{1}{9}(C_{11} + C_{22} + C_{33}) + \frac{2}{9}\ (C_{12} + C_{13} + C_{23})$$

(1)

$$G = \frac{1}{15}[(C_{11} + C_{22} + C_{33}) - (C_{12} + C_{13} + C_{23})] + \frac{1}{5}(C_{44} + C_{55} + C_{66})$$

(2)

$$E = \frac{9KG}{(3K+G)}$$

(3)

However, the authors **[23]** mentioned, that in the tetragonal system such as the γ-phase, there are six independent elastic constants viz. (c11=c22, c12; c13=c23,c33; c44=c55,c66). As a result, the elastic modulus equation of the tetragonal system can be written as:

$$K = \frac{1}{9}(2C_{11} + C_{33}) + \frac{2}{9}\ (C_{12} + 2C_{13}$$

(4)

$$G = \frac{1}{15}(2C_{11} + C_{33} - C_{12} + 2C_{13} + 6C_{44} + 3C_{66})$$

(5)

2.3 Sample preparation

The chemical analysis of the γ-TiAl based alloy illustrating both the nominal and final material's composition is shown in **Table 1**. The alloy was first generated as precursor metallic powders of pure Ti, Al, Nb, Cr, and Si. A 50g charge alloy sample was blended for two hours in a tubular mixer, with subsequent uniaxial cold pressing (380 MPa) in a cylindrical 43 mm diameter dies. Lastly, the compacted alloy was melted using an arc melting furnace, which uses an electric arc under a protective high purity argon atmosphere, and solidified in a copper hearth. The difference between the raw materials composition with that of the final composition (**Table 1**), may be due to different vapour pressures of different components via melting process, whereby Al (low melting point) being volatile may have suffered the most burning loss.

Metallographic preparation was carried out using conventional techniques. Specimen surfaces were ground to a mirror-like surface using grit papers up to 4000 followed by 1 µm alumina, colloidal silica and then etched in 24ml H2O + 50ml glycerol +24ml HNO_3 + 2ml HF. The scanning electron microscope (SEM) was used to reveal the microstructure of the alloys. However, in order to determine microstructural analysis on the as-cast Ti-45Al-2Nb-0.7Cr-0.3Si alloy, the SEM with electron backscatter diffraction (EBSD) was utilised. Due to complexity of the phases in the alloy (i.e. γ-tetragonal, α_2-hexagonal, precipitate-Ti_5Si_3) computer simulation techniques using first principles density functional theory especially the determination of atomic positions (Wyckoff notations) was conducted, in order to enable accessing crystallographic data on the twist software, while proceeding with the EBSD analysis. The specimen analysed for EBSD was mechanically polished up-to colloidal silica and electro-polished in a solution of 600 ml methanol, 360 ml butoxyethanol and 60 ml perchloric acid. The parameters used to conduct EBSD analysis: (i) acceleration voltage was 20kV, and (ii) the specimen tilted at angle of 70 ^{0}. The common way to distinguish EBSD is its colour representation which is used as a tool to visualise local crystal orientations, which are expressed in Euler angles ($\varphi_1\phi\varphi_2$), which is therefore a representation of successive conventional rotations to match the crystal orientation with a Cartesian co-ordinate system related with sample surface **[12]**. In addition, the research study discusses briefly the crystallographic textures which is beyond the scope of the study; however, the focus will be on relative disorientations between pixels of a given mapped surface.

3. Results and discussion

3.1 First-principles method

Fig. 1: Top image is 32-atom TiAl supercell. Red and green spheres represents Ti and Al atoms, respectively, Bottom image is the crystal structures in B2-contained TiAl alloy (a) Hexagonal α_2-Ti_3Al phase (DO19); (b) Tetragonal γ-TiAl phase (L10); (c) Cubic B2 contained TiAl alloy (a) Hexagonal α_2-Ti_3Al phase (DO19); (b) Tetragonal γ-TiAl phase (L10); (c) Cubic B2 phase **[12].**

A first principle supercell approach is used to obtain the formation of enthalpies of isolated point defects in $L1_0$ TiAl, as such a 32-atom 2×2×2 super-cells in **Fig.1** has been employed **[12]**, whereby each cell contains a single point defect (vacancy, antisite or ternary element in its center). In the current study, the semi-core 3p electrons of Ti, Cr, and the semi-core 4p electrons of Nb; the interstitial atoms of Si are explicitly treated as valence. However, the plane wave cutoff energy is set at 500 eV. Whereas, the k-point meshes for Brillouin zone sampling are constructed using the Monkhorst-Pack scheme, and a 9×9×9 k-point mesh for the 32-atom supercell (corresponding to 75 irreducible k-points in the Brilloiun zone) is found to be sufficient to give fully converged point defect energetics. **Table 2** represents crystallographic data of the investigated crystal structures L10, D019 and B2 of the TiAl based alloys.

Table 1: Crystallographic data of stable and metastable constituents in Ti-Al intermetallic alloys **[20].**

The current investigation is comprised of the Ti-45Al-2Nb-0.7Cr-0.3Si (at. %) invariably composed of the Ti_5Si_3 precipitate in as-cast and heat-treated condition with the hexagonal closed packed (HCP) crystal structure of Mn_5Si_3 prototype with a space group of $P6_3/mcm$. The calculated lattice parameters of Ti-45Al-2Nb-0.7Cr-0.3Si intermetallic alloy are comparable to the experimental data indicated in **Table 2**, which were found to be: γ-phase, $a=b=2.81295$ Å, $c=4.08134$ Å, with $\alpha/\gamma/\beta$ angle=90. The α_2 phase $a=b=5.72989$ Å, c=4.64225 Å, whereby the $\alpha/\gamma=90^0$,

$\beta=120^0$. The structure of γ-TiAl based alloys was reviewed in detail by Braun et al., **[24]**.

The substitution of atoms changes the crystal structure lattice parameters due to differences in atomic radius, electronegativity etc. The calculated positions of the TiAl atoms are presented in **Table 3** denoted by the Pearson symbol *tP2*. **Table 4** represents α_2-Ti_3Al which is a closed packed hexagonal crystal structure denoted by Pearson symbol *hP8* (which resembles the α crystal structure) while **Table 5** represent atomic positions of the supposedly Ti_5Si_3 precipitate in the Ti-45Al-2Nb-0.7Cr-0.3Si alloy. Furthermore, it was suggested that Ti_5Si_3 particles stable at room temperature in the Ti-45Al-2Nb-0.7Cr-0.3Si alloy may have precipitated from the liquid during the melting process **[3]**. The geometry optimization for the precipitate and the calculated lattice parameters with their respective co-ordinate angles are $a=b=7.445$Å, $\alpha=\beta=90$; and $c=5.143$Å, $\gamma=120$. Therefore, the atomic positions and occupancy numbers was helpful for inciting the atomic positions of the predicted room temperature phases after casting into the EBSD equipment software.

Table 2: Atomic positions (Wyckoff notation) in the L10 TiAl crystal structure.

Table 3: Atomic positions (Wyckoff notation) in the DO19 Ti_3Al crystal structure.

Table 4: Atomic positions (Wyckoff notation) in the Ti5Si3 crystal structure.

Solidification and phase transformation depends on the alloy composition. It is believed that the γ-phase lamellae start precipitating inside coarse parent α-peritectic grains in the Blackburn orientation relationship (BOR):

$\{111\}_\gamma \parallel (0002)_\alpha$ and

$<1\ \bar{1}\ 0>_\gamma \parallel <1\ 1\ \bar{2}\ 0>_\alpha$.

Moreover, towards the last stage of cooling, the untransformed α-phase inside the lamellar structure becomes ordered α_2-phase with the same orientation. The α_2 lamellae coexist with γ-tetragonal lamellae presenting six different crystallographic orientations called variants. Often the γ/γ and γ/α_2 interfaces are found in lamellar structures **[25]**. On the other hand, Hecht et al., **[26]** reported α-Ti forming along peritectic reaction and transformation path by solid state growth from single phase β-Ti via both mechanisms. The solidification and phase transformation path is strongly depended on alloy composition and on solidification kinetics and nucleation behaviour of α-Ti **[26]**. The calculated geometry optimization was performed on α-Ti and the lattice parameters with their respective co-ordinate angles viz. the $a=b=3,202$ Å, $\alpha=\beta=90$; and $c=5.199$ Å, $\gamma=120$ which is comparable to the experimental data in **Table 2**. The atomic position of α-Ti is the same as the α_2 which is represented in **Table 4**.

3.2 SEM-EBSD microstructure analysis

Transformation mechanism in the as-cast microstructure confirms the $(\gamma+\alpha_2)$ phases with the Ti_5Si_3 particles situated near the γ/α_2 interface boundaries **[27]**. Its XRD results indicated the pattern exhibiting several diffraction peaks belonging to α-Ti_3Al and γ-TiAl and minor peaks of the Ti_5Si_3 second phase **[27]**.

Fig.2: EBSD results of the as-cast Ti-45Al-2Nb-0.2Cr-0.3Si alloy: (a) SEM-EBSD band contrast map (based upon quality of the acquired Kikuchi patterns); (b) Euler angles; (c) phase constituents; (d)-(f) orientation maps mainly indicating the inverse pole figures.

Fig.2 illustrates the EBSD results of the as-cast Ti-45Al-2Nb-0.7Cr-0.3Si alloy. As shown in **Fig.2a**, the SEM-EBSD band contrast image based on the quality of Kikuchi patterns on each point on the mapped surface. **Fig.2b** is an indication of the three Euler angles which describes the orientation of the crystal lattice as determined by the indexing procedure. **Fig. 2c** represents phase constituents which exhibited $\gamma/\alpha_2/Ti_5Si_3$ phases in the analysed area marked by green, yellow and blue (α_2-with different lattice parameters shown in **Table 7**), and pink colours. **Fig 2 (d)-(f)** is a representation of orientation map superimposed with band contrast image of **Fig 2a**, with their corresponding inverse pole figures in the x, y and z direction. The boundaries between lamellar grains are often escorted with equiaxed γ-mono grains **[25]**. However, in this case the lamellar grains were identified having mostly the γ-phase (~90%), which is supported by phase fraction estimation shown in **Table 6**.

Fig.3: (a) an electron layered image of an electro-polished Ti-45Al-2Nb-0.7Cr-0.3Si intermetallic alloy (c), (e) and (g) are Kikuchi patterns with their corresponding indexed phases (b), (d), (f) and (h) according to the colour coding.

Fig.3a represents EBSD layered image which stems from phase constituent (as marked by different colours) in **Fig. 2c**. The phase fraction estimation is illustrated in **Table 6**, where mean angular deviation (MAD) describe the perfection of the fit of the solution. According to CHANNEL 5 oxford instrument **[28]**, the smaller the MAD number, the better the match between the detected Kikuchi bands and the simulation. In general, a number under 1^0 is acceptable for most systems. As depicted in **Table 6**, the phase with better matching of the Kikuchi patterns is the γ-phase structure. As shown in **Fig. 3 c, e, g** are the Kikuchi patterns with corresponding indexed phases **(Fig.3 b, d, f and h).** The structural data is depicted in **Table 7**. The Ti_5Si_3 phase is found along the γ-grain boundaries **[27]**. The lattice parameters in **Table 7** yields *c/a*=1.4520 for the γ-TiAl while that of Ti_5Si_3 is 0.6899 similar to that published by Sun et al **[29]**.

Table 5: Phase fraction estimation

Table 6: Phase acquisition

3.3 Crystallography of phase domains

Fig.4: Contoured pole figures (a) γ-phase, and (b) α-phase

According to Yang et al **[30]**, the misorientation angles between the α-grains arising from the same β-grain can only be $10^{0}\ 53'$, 60^{0}, $60^{0}\ 83'$, $63^{0}\ 26'$, or 90^{0}, respectively. Furthermore, the misorientation angles measured by EBSD between neighbouring α-grains differ from these ordinates, implying that these grains cannot originate from the same parent β-grain hence the transformation will not obey the burgers orientation relationship **[26]**:

$\{110\}^{\beta} // \{0001\}^{\alpha}$

$<111>^{\beta} // <2\ \bar{1}\ \bar{1}0>^{\alpha}$

Therefore, the orientation angle can be applied to ascertain whether the α grain obeys the Burgers orientation relationship or not. In addition, when the misorientation angles between the neighbouring α-grains differ from other angles, these grains are non-Burgers α-grains, as such the microstructure is regarded to be non-textured. On the other hand, misorientation axes in crystal coordinate system help to clarify which crystallographic directions the misorientation axes align with for a given range of misorientation angles. As shown in **Fig. 5a, 6a and 7a** the misorientation axes in the form of four colours sketches the $\alpha/\alpha_2/\gamma$ grain boundaries and captures the orientation difference of neighbouring grains viz. (8^{0}-12^{0}, blue; 57^{0}-63^{0},green to yellow; 88^{0}-92^{0}, red); inverse pole figures. **Fig.2c** illustrates two colours viz. green and red representing the γ and α-phase, respectively; in order to highlight all pixels of the EBSD map where the orientation is close within an angular tolerance of 20^{0} related to γ-variants of the lamellae in the structure. **Fig.4** shows the contoured pole figures between the γ + α-phases; illustrating {111} // {10-10} following the black burn orientation. The spatial and angular resolutions of transmission microscopy are required to distinguish the different γ-lamellae and its variants **[25]**.

Fig.5: Misorientation data on the γ-phase: (a) Misorientation axes of the γ-phase with corresponding colour coding; (b) Misorientation angle distribution; and (c) <111> fiber texture.

The Blackburn orientation relationship at interface between γ and α phase belongs to:

$$(111)\gamma \,||\, (0001)\alpha \text{ and } <1\ \bar{1}0]\gamma \,||\, <11\ \bar{2}0>\alpha$$

Therefore this may stipulate that the γ-phase precipitated from the α-phase. On the other hand, **Fig.5a** shows misorientation axes in crystal co-ordinate system of the γ-phase, this describes which crystallography directions the misorientation axes align with for a chosen range of misorientation angles. Misorientation axes are observed indicated by clusters between [001] and [010] in the 57-63^0 section; another cluster is observed at about the [110] in the 88-92^0. This may be supplemented by **Fig.5b** which is a representation of the relative frequency vs. misorientation angle, where the correlated blue and uncorrelated red misorientation plot are different from the random line and from each other. The difference between the uncorrelated and random distribution may be due to the strong fiber texture <111> shown in **Fig.5c** where coloured grains in the texture map are Burgers γ grains and others are non-Burgers γ-grains. The correlated distribution exhibits a fairly large number of boundaries with misorientations below 15^0 compared to the uncorrelated distribution. Moreover, the results also show that the correlated distribution exhibiting large number of boundaries with misorientations enclosed by 85-90^0. Clearly from these results, the low and high angle boundary may be a significant feature of the microstructure and not simply a product of strong texture.

Fig.6: (a) Misorientation axes of the α_2-phase with corresponding colour coding; (b) Misorientation angle distribution (α_2); (c) Pole figures: i) of γ-phase, ii) α_2-phase and iii) α-parent phase; and (d) the <110> fiber texture (α_2)

Fig.6a shows the misorientation axes of the α_2 phase, where clusters are seen between <011> and <010> in the 8-12^0 angle, whereas clusters <010> are observed in the 35-42^0 angle, also clustering of <101> in the 57-63^0 and lastly clusters of <120> in the 88-92^0. **Fig 6b** is the representation of the misorientation angle, where the correlated distribution exhibits a fairly large number of boundaries with misorientations below 15^0 compared to the uncorrelated distribution. Like the γ-phase, it can be seen that the low angle boundary might be a significant feature of the microstructure and not a product of texture in **Fig.6d**. **Fig.6c** (i) is the γ-pole figure {110} parallel to the α_2-phase in the <110> direction shown in **Fig.6c** (ii), as indicated by the blue circles. The two phases may exhibit a Burgers orientation relationship with the parent α-phase, also represented by the blue circle in **Fig.6c** (iii) which illustrates the α pole figure in the <0001> direction.

Fig.7: (a) Misorientation axes of the Ti_5Si_3 second-phase with corresponding colour coding; (b) Misorientation angle distribution (Ti_5Si_3); Pole figures of (c) α, and (d) (Ti_5Si_3)

Fig.7a shows the misorientation axes with accompanying colour coding of the Ti_5Si_3 precipitate; there are no observable clusters of direction in the respective angles. However, like the α_2-phase, the misorientation angles of the precipitate (**Fig.7b**) exhibits a large number of boundaries with misorientation below 15^0. The results indicate that there is no preferential misorientations found in the second phase in the as-cast condition. The pole figures of α-phase and the precipitate Ti_5Si_3 seems to obey the orientation relationship, and the precipitate nucleated from the α-phase. It follows $L \rightarrow \beta + L_1$ relationship while cooling takes place, eutectic reaction occurs at about 1432 ^{0}C corresponding with $L_1 \rightarrow \alpha + Ti_5Si_3$. However, dendrites present in the in as-cast microstructure exhibiting a hexagonal symmetry of the α-dendrites, which is suggestive of a reaction $L1 + \beta \rightarrow \alpha$ that occurred immediately after solidification of $L \rightarrow \beta + L1$. Among these dendrites, the eutectic reaction $L1 \rightarrow \alpha + Ti_5Si_3$ occurred in the last solidified liquid (Si-rich) **[31]**.

3.4 Heat-treated fully lamellar structure

Fig.8: SEM/BSE micrograph showing a fully lamellar structure of the Ti-45Al-2Nb-0.7Cr-0.3Si

Fig. 8 illustrates a fully lamellar structure of the Ti-45Al-2Nb-0.7Cr-0.3Si intermetallic alloy from the α-phase domain with subsequent furnace cooling after heat-treatment process. The phase acquisition was done employing the XRD results revealing fully lamellar structure of the γ- Ti-45Al-2Nb-0.7Cr-0.3Si alloy **[27]**.

Fig.9: EBSD map of the fully lamellar Ti-45Al-2Nb-0.7Cr-0.3Si alloy: (a) Electron micrograph, (b) Band contrast image, (c) grain orientation map, and d) phase colour map.

To characterise this heat-treated fully lamellar Ti-45Al-2Nb-0.7Cr-0.3Si alloy, EBSD method was adopted. **Fig. 9a** represent a backscattered electron image while the band contrast is shown **Fig. 9b**. The grain orientation in **Fig. 9c** of the lamellar (γ+α_2) structure are almost random, associated with no texture attainable in the fully lamellar structure. **Fig. 9d** is the phase colour map, with the evidence that the γ-phase is dominating phase with a *c/a* ratio of 1.452.

4. Conclusion

The following conclusions are drawn:

- First principle approach (using VASP) was performed to study the stability of $L1_0$, DO19 and HCP-A3 atomic position. Moreover, the Wyckoff notation and occupancy numbers obtained for the phases were used for the EBSD analysis.
- The calculated lattice parameters are in good agreement with the available experimental data.
- Grain orientation of $\gamma/\alpha/Ti_5Si_3$ phases were studied via EBSD, using its distinctive advanced fit band detection and indexing algorithm, the HKL CHANNEL 5 invariably and correctly measured the orientation of the tetragonal γ-TiAl crystals. Additionally, interphase boundaries of the $\gamma/\alpha_2/Ti_5Si_3$ were investigated.
- It has been shown that the formation of $\gamma/\alpha_2/Ti_5Si_3$ in the Ti-45Al-2Nb-0.7Cr-0.3Si intermetallic alloy followed the Blackburn orientation relationship. According to Zambaldi **[32]**, this relation is precisely followed by $<1\bar{1}0]$ direction, while the $<\bar{1}01]$ directions show deviations of 0.2^0 to 0.3^0 to the respective α_2-directions.

- It was also shown that the Ti_5Si_3/γ interface has an orientation relationship of $(011)_{\gamma}$ || $(0110)_{Ti5Si3}$ and $(233)_{\gamma}$ || $(0002)_{Ti5Si3}$.
-

5. Acknowledgements

Department of Science and Technology (DST) and Council of Scientific Industrial Research (CSIR) is acknowledged for funding this work. Finally, the technical support from the University of Pretoria mainly for the provision of some of the laboratory equipment’s. We are thankful to Dr. R Modiba for her fruitful discussing in first principle calculation data.

6. References

[1] G. Baudana, S. Biamino, B. Kloden, A. Kirchner, T. Weißgarber, B. Kieback, M. Pavese, D. Ugues, P. Fino, C. Badini, Electron Beam Melting of Ti-48Al-2Nb-0.7Cr-0.3Si: Feasibility investigation, Intermetallics, 73 (2016) 43–49.

[2] K. Kothari, R. Radhakrishnan, N. M. Wereley, Advances in gamma titanium aluminides and their manufacturing techniques, Prog Aerosp Sci. 55 (2012)1–16.

[3] T. Klein, L. Usategui, B. Rashkova, M.L. N, J. San Juan, H. Clemens, S. Mayer, Mechanical behavior and related microstructural aspects of a nano-lamellar TiAl alloy at elevated temperatures, Acta Mater. 128 (2017) 440-450.

[4] A.M. Abd El-Rahman, M.F. Maitz, M. A. Kassem, F.M. El-Hossary, F. Prokert, H. Reuther, M. T. Pham, E. Richter, Surface improvement and biocompatibility of TiAl24Nb10 intermetallic alloy using rf plasma nitriding, Appl Surf Sci. 253 (23) (2007) 9067–9072.

[5] S. R. Chubb, D. A. Papaconstantopoulos, B. M. Klein, First-principles study of L10 Ti-Al and V-Al alloys, Phys. Rev. B 38 (17) (1988) 12120–12124.

[6] T. Popela, D. Vojtecha, J. B. Vogt, A. Michalcová, Structural, mechanical and oxidation characteristics of siliconized Ti–Al–X (X = Nb, Ta) alloys, Appl Surf Sci. 307 (2014) 579–588.

[7] J. Fan, X. Li, Y. Su, J. Guo, H. Fu, Dependency of microhardness on solidification processing parameters and microstructure characteristics in the directionally solidified Ti-46Al-0.5W-0.5Si alloy, J. Alloys Compd. 504 (1) (2010) 60–64.

[8] M. Palm, N. Engberding, F. Stein, K. Kelm, S. Irsen, Phases and evolution of microstructures in Ti–60 at.% Al, Acta Mater. 60 (8) (2012) 3559–3569.

[9] K. Xia, X. Wu, D. Song, Effects of Gd addition, lamellar spacing and loading direction on creep behaviour of a fully lamellar Ti–44Al–1Mn–2.5Nb alloy, Acta Mater.52 (4) (2004) 841–849.

[10] D. R. Johnson, Y. Masuda, H. Inui, M. Yamaguchi, Alignment of the TiAl/Ti_3Al lamellar microstructure in TiAl alloys by growth from a seed material, Acta Mater. 45 (6) (1997) 2523–2533.

[11] F. Herrouin, D. Hu, P. Bowen, I. P. Jones, Microstructural changes during creep of a fully lamellar TiAl alloy, Acta Mater. 46 (14) (1998) 4963–4972.

[12] Y. Jin, J. N. Wang, J. Yang, Y. Wang, Microstructure refinement of cast TiAl alloys by beta solidification, Scr. Mater. 51 (2) (2004) 113–117.

[13] D. X Wei, Y. Koizumi, M. Nagasako, A. Chiba, Refinement of lamellar structures in Ti-Al alloy, Acta Mater. 125 (2017) 81-97.

[14] X. Li, F. Bottler, R. Spatschek, A. Schmitt, M. Heilmaier, F. Stein, Coarsening kinetics of lamellar microstructures: Experiments and simulations on a fully-lamellar Fe-Al in situ composite, Acta Mater.127 (2017) 230-243.

[15] S. Cao, S. Xiao, Y. Chen, L. Xu, X. Wang, J. Han, Y. Jia, Phase transformations of the L12-Ti_3Al phase in γ-TiAl alloy, Mater. Des.121 (2017) 61–68.

[16] R. Guo, P. Shen, C. Sun, Y. Wang, A. Shaga, Q. Jiang, Processing and mechanical properties of lamellar-structured Al–7Si–5Cu/TiC composites, Mater. Des. 106 (2016) 446–453.

[17] J. Ning, Y. Zhang, L. Huang, Y. Feng, Stabilized uniform deformation in a high-strength ferrite-cementite steel with multiscale lamellar structure, Mater. Des. 120 (2017) 280–290.

[18] A. Mohammad, A.M. Al-Ahmari, V. K. Balla, M. Das, S. Datta, D. Yadav, G.D. Janaki Ram, In vitro wear, corrosion and biocompatibility of electron beam melted γ-TiAl, Mater. Des. 133 (2017) 186–194.

[19] C. Jiang, First-principles study of site occupancy of dilute 3d, 4d and 5d transition metal solutes in L10 TiAl, Acta Mater. 56 (20) (2008) 6224–6231.

[20] C. Z. Qiu, Y. Liu, L. Huang, B. Liu, W. Zhang, Y. H. He, B. Y. Huang, Tuning mechanical properties for (B2)-containing TiAl intermetallics, Trans. Nonferrous Met. Soc. China. 22 (11) (2012) 2593–2603.

[21] S. Plimpton, Fast Parallel Algorithms for Short–Range Molecular Dynamics, Phys. Rev. B. 117 (1995) 1–19.

[22] H. Monkhorst, J. D. Pack, On Special Points for Brillouin Zone Integrations, Phys. Rev. B. 13 (1976) 5188–5192.

[23] Y. Kang, Y. Han, S. Qu, J. Song, Effects of Alloying Elements Ti, Cr, Al, and Hf on β-Nb5Si3 from First-principles Calculations, Chinese J. Aeronaut. 22 (2) (2009) 206–210.

[24] J. Braun, Ellner, B. Predel, Experimental investigations of the structure and stability of the TiAl phase. Zeitschrift fur Metallkunde.86 (12) (1995) 870–876.

[25] S. R. Dey, A. Hazotte, E. Bouzy, Crystallography and phase transformation mechanisms in TiAl-based alloys – A synthesis, Intermetallics 17 (12) (2009) 1052–1064.

[26] U. Hecht, V. Witusiewicz, A. Drevermann, J. Zollinger, Grain refinement by low boron additions in niobium-rich TiAl-based alloys” Intermetallics, 16 (8) (2008) 969–978.

[27] M. N Mathabathe, A. S Bolokang, G. Govender, R.J. Mostert, C. W Siyasiya, The vacuum melted ɣ-TiAl (Nb, Cr, Si)-doped alloys and their cyclic oxidation properties, Vacuum. 154 (2018) 82–89.

[28] Oxford, “Oxford Instruments CHANNEL 5,” *User Man.*, 2010.

[29] F. S. Sun, S. E. Kim, C. X. Cao, Y. T. Lee, M. G. Yan, A study of Ti_5Si3/gamma interface in TiAl alloys, Scr. Mater. 45 (2001) 383–389.

[30] G. Yang, H. Kou, J. Yang, J. Li, H. Fu, Microstructure control of Ti-45Al-8.5Nb-(W,B,Y) alloy during the solidification process, Acta Mater. 112 (2016) 121–131.

[31] F. Sun, F. H. S. Froes, Solidification behaviour of Ti_5Si_3 whiskers in TiAl alloys, Mater. Sci. Eng. A. 345 (2003) 262–269.

[32] C. R. Zambaldi, Micromechanical modeling of γ -TiAl based alloys. PhD Dissertation, Deutschen Nationalbibliografie, (2010) 1-201.

Table 1: Chemical composition of the γ-TiAl based alloy

Elements	**Nominal composition (at. %)**	**As-melted final composition (at. %)**
Ti	49	51.68
Al	48	45.4
Nb	2	1.92
Cr	0.7	0.73
Si	0.3	0.27

Table 2: Crystallographic data of stable and metastable constituents in Ti-Al intermetallic alloys **[20].**

Alloy	**Density/ (mg.m^{-3})**	**Cell parameter**			**Pearson symbol**	**Space group**	**Crystal structure**
		a/nm	c/nm	γ/(°)			
β(ht Ti)	4.31	0.333	0.333	90	cI2	Im3m	BCC-A2
α(RT tI)	4.12	0.289.	0.464	120	hP2	P6$_3$/mmc	HCP-A3
α2(Ti$_3$Al)	4.22	0.578	0.465	120	hP8	P6$_3$/mmc	DO$_{19}$
γ(TiAl)	3.82	0.283	0.407	90	tP2	P4/mmm	L1$_0$
B2(TiMo$_{0.5}$Al$_{0.5}$)	5.63	0.318	0.318	-	-	-	-
B2(TiNb$_{0.5}$ Al$_{0.5}$)	4.75	0.324	0.324	90	cP2	Pm3m	B2
B2(TiCr$_{0.3}$ Al$_{0.7}$)	4.55	0.312	0.312	-	-	-	-

*a=b and $\alpha=\beta=90^0$. The values of density and (a, b, c) will change after alloying with some other different elements

Table 3: Atomic positions (Wyckoff notation) in the L10 TiAl crystal structure.

Structure	**Atom**	**Positions**	**X**	**Y**	**Z**	**Occupancy**

						Number
L1$_0$	Al 1	1d	0.5	0.5	0.5	1
	Ti 1	1a	0.0	0.0	0.0	1

Table 4: Atomic positions (Wyckoff notation) in the DO19 Ti_3Al crystal structure.

Structure	**Atom**	**Positions**	**X**	**Y**	**Z**	**Occupancy Number**
DO_{19}	Ti 1	6h	0.16953	0.33906	0.25000	1
	Al 1	2d	0.33333	0.66667	0.75000	1

Table 5: Atomic positions (Wyckoff notation) in the Ti5Si3 crystal structure.

Structure	Atom	Positions	X	Y	Z	Occupancy Number
Hexagonal Ti_5Si_3	Ti1	6g	0.236	0.000	0.250	1
	Si1	6g	0.599	0.000	0.250	1
	Ti2	4d	0.333	0.667	0.000	1

Table 6: Phase fraction estimation

Phase Name	Phase Fraction (%)	Phase Count	Mean Band Contrast	Standard Deviation Band Contrast	Mean MAD	Standard Deviation MAD
Alpha	0.33	76	103.62	11.57	1.15	0.37
(Ti_3Al)	0.05	12	110.08	17.43	1.26	0.42
Alpha 2	4.56	1037	109.94	15.60	0.88	0.39
Gamma	89.84	20439	157.74	22.05	0.63	0.18
Ti_5Si_3	0.73	165	131.65	19.89	0.74	0.24
Zero Solutions	4.49	1021	114.80	23.17		

Table 7: Phase acquisition

Phase Name	**a**	**b**	**c**	**α**	**β**	**γ**	**Space group**
Alpha	3.20 Å	3.20 Å	5.20 Å	90.00 °	90.00 °	120.00 °	194
(Ti_3Al)	5.72 Å	5.72 Å	4.64 Å	90.00 °	90.00 °	120.00 °	194
Alpha 2	5.73 Å	5.73 Å	4.64 Å	90.00 °	90.00 °	120.00 °	194
Gamma	2.81 Å	2.81 Å	4.08 Å	90.00 °	90.00 °	90.00 °	123
Ti_5Si_3	7.45 Å	7.45 Å	5.14 Å	90.00 °	90.00 °	120.00 °	193

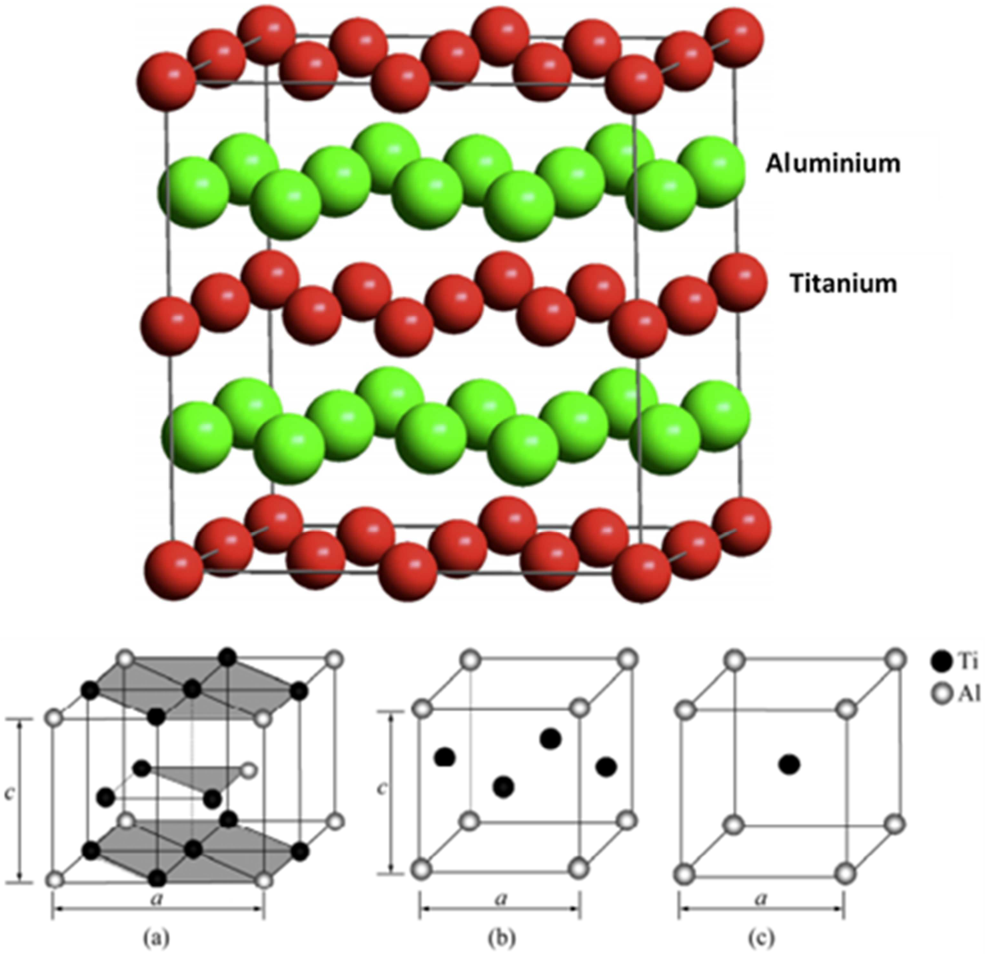

Fig. 1: Top image is 32-atom TiAl supercell. Red and green spheres represents Ti and Al atoms, respectively, Bottom image is the crystal structures in B2-contained TiAl alloy (a) Hexagonal α_2-Ti_3Al phase (DO19); (b) Tetragonal γ-TiAl phase (L10); (c) Cubic B2 contained TiAl alloy (a) Hexagonal α_2-Ti_3Al phase (DO19); (b) Tetragonal γ-TiAl phase (L10); (c) Cubic B2 phase **[12].**

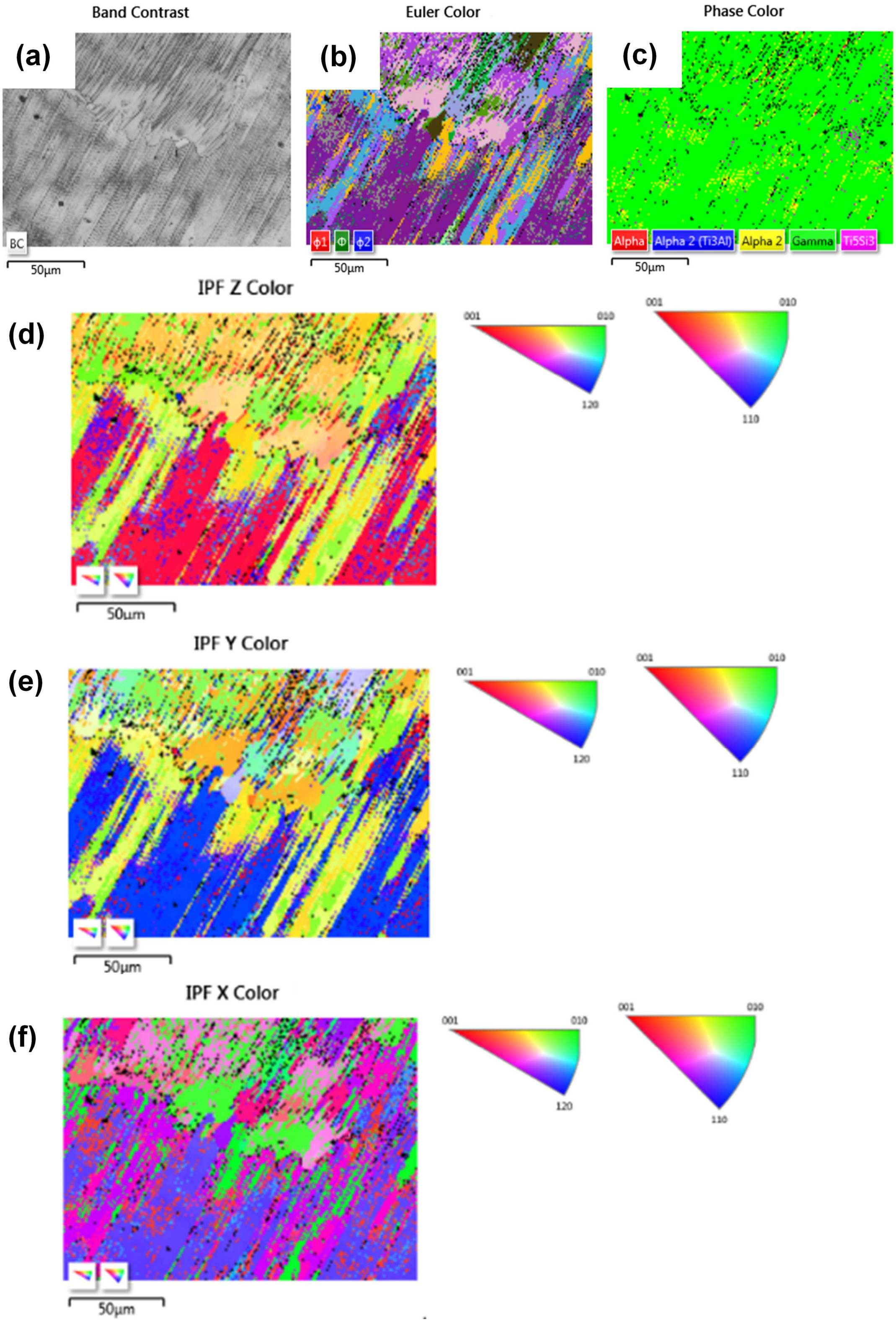

Fig.2: EBSD results of the as-cast Ti-45Al-2Nb-0.2Cr-0.3Si alloy: (a) SEM-EBSD band contrast map (based upon quality of the acquired Kikuchi patterns); (b) Euler angles; (c) phase constituents; (d)-(f) orientation maps mainly indicating the inverse pole figures.

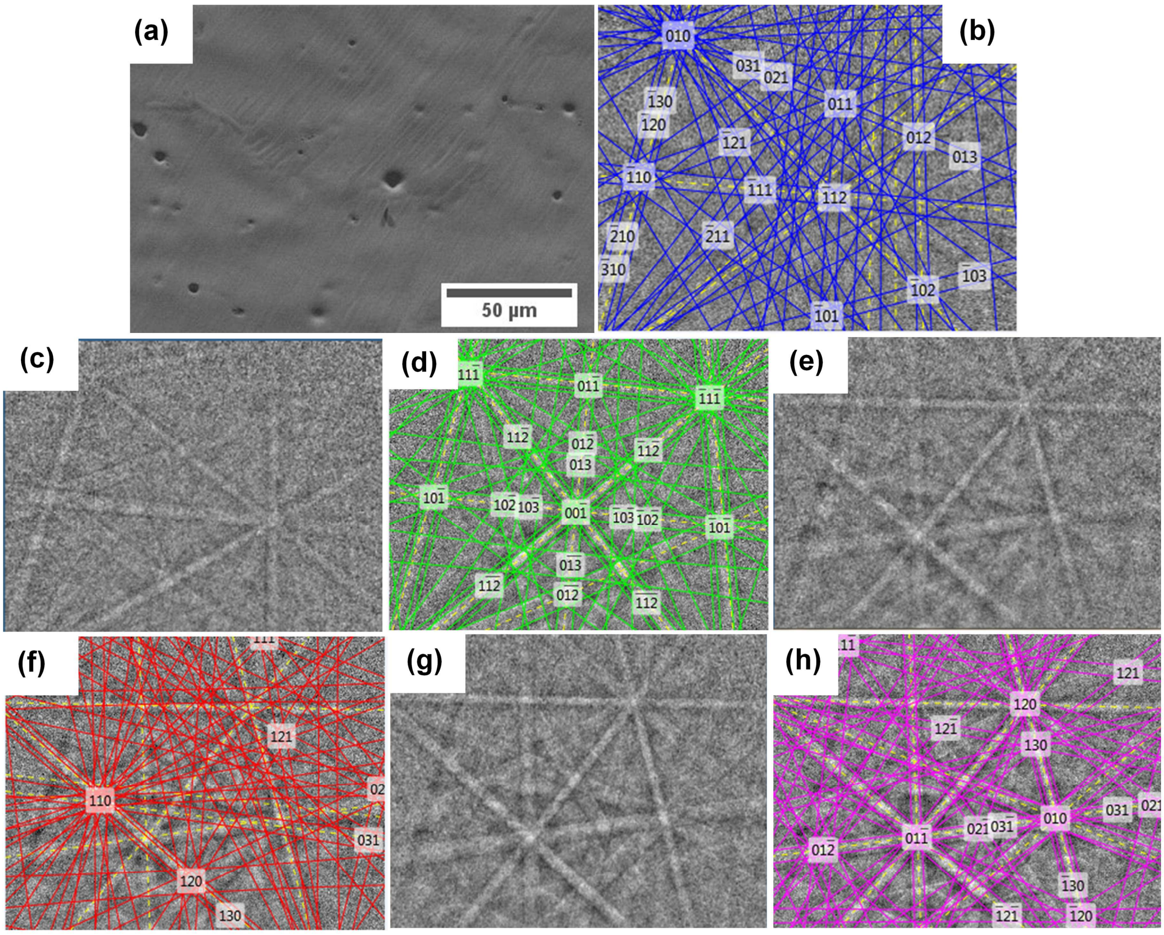

Fig.3: (a) an electron layered image of an electro-polished Ti-45Al-2Nb-0.7Cr-0.3Si intermetallic alloy (c), (e) and (g) are Kikuchi patterns with their corresponding indexed phases (b), (d), (f) and (h) according to the colour coding.

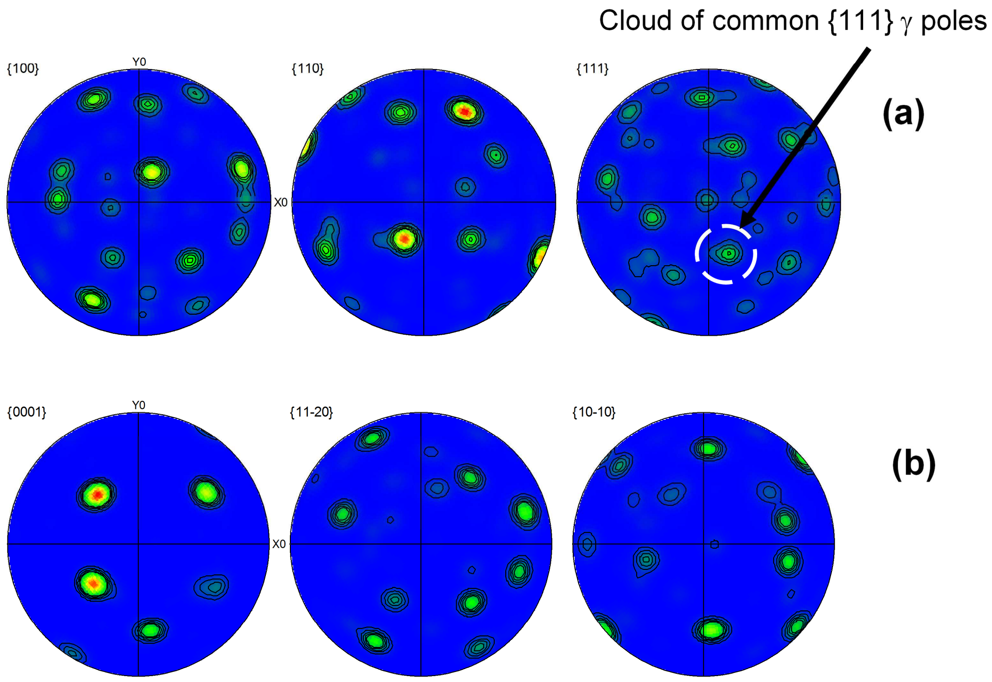

Fig.4: Contoured pole figures (a) γ-phase, and (b) α-phase

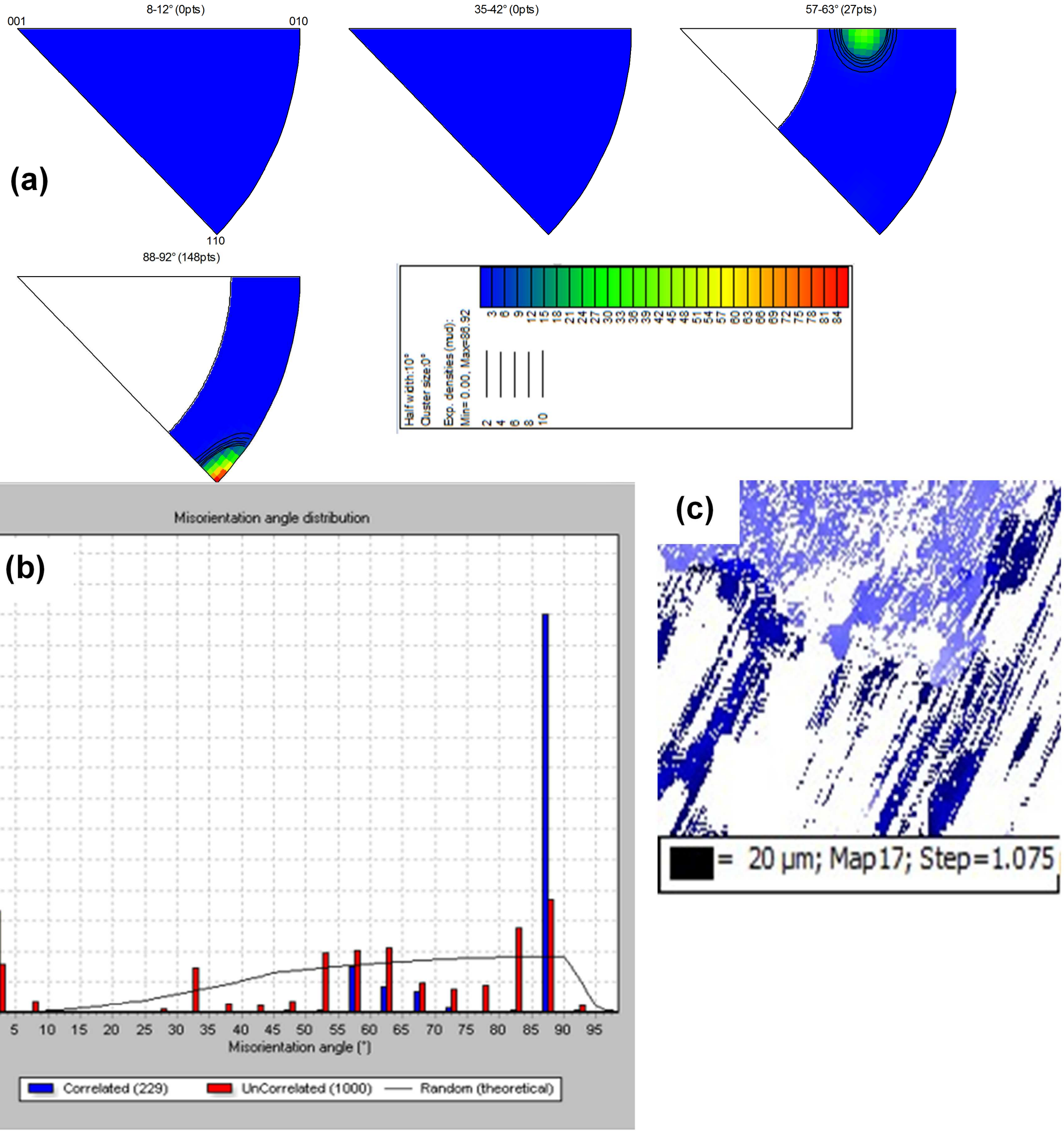

Fig.5: Misorientation data on the γ-phase: (a) Misorientation axes of the γ-phase with corresponding colour coding; (b) Misorientation angle distribution; and (c) <111> fiber texture.

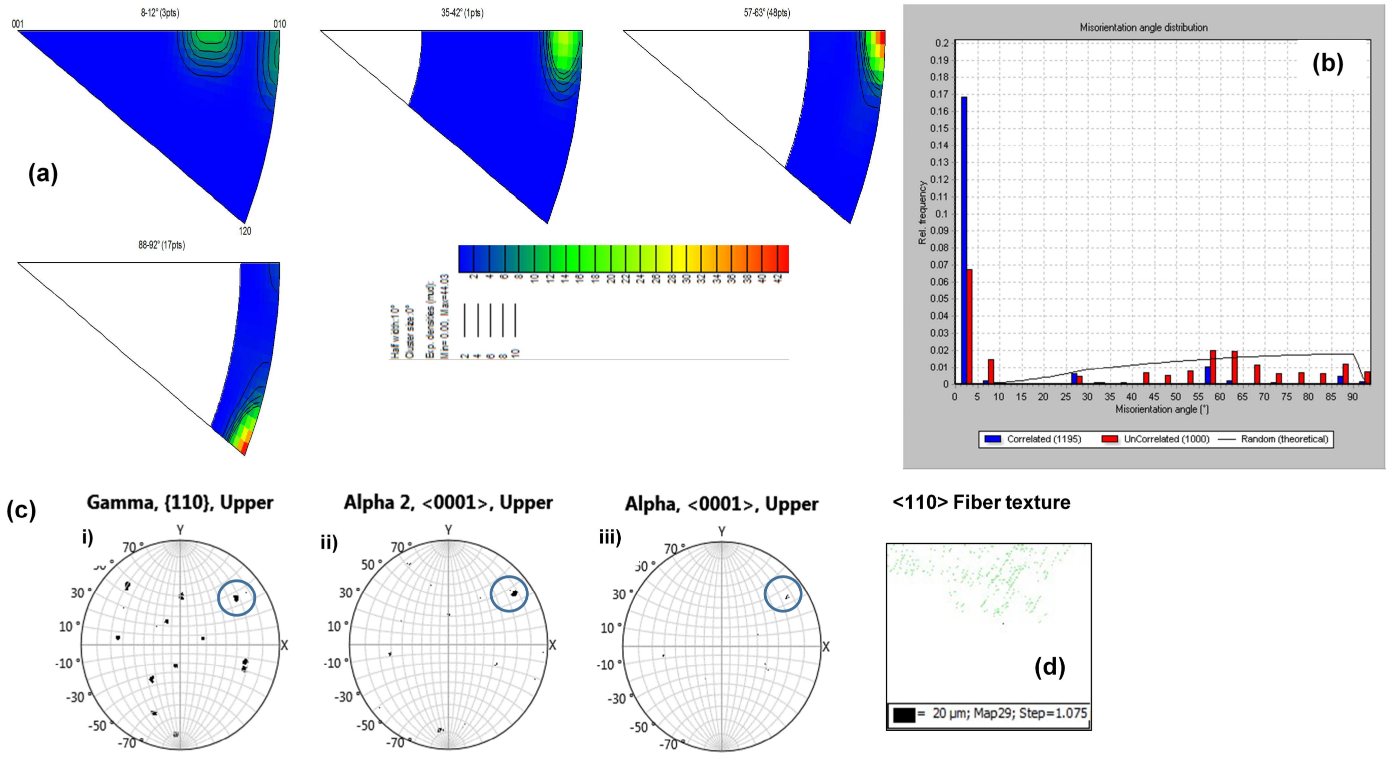

Fig.6: (a) Misorientation axes of the α_2-phase with corresponding colour coding; (b) Misorientation angle distribution (α_2); (c) Pole figures: i) of γ-phase, ii) α_2-phase and iii) α-parent phase; and (d) the <110> fiber texture (α_2)

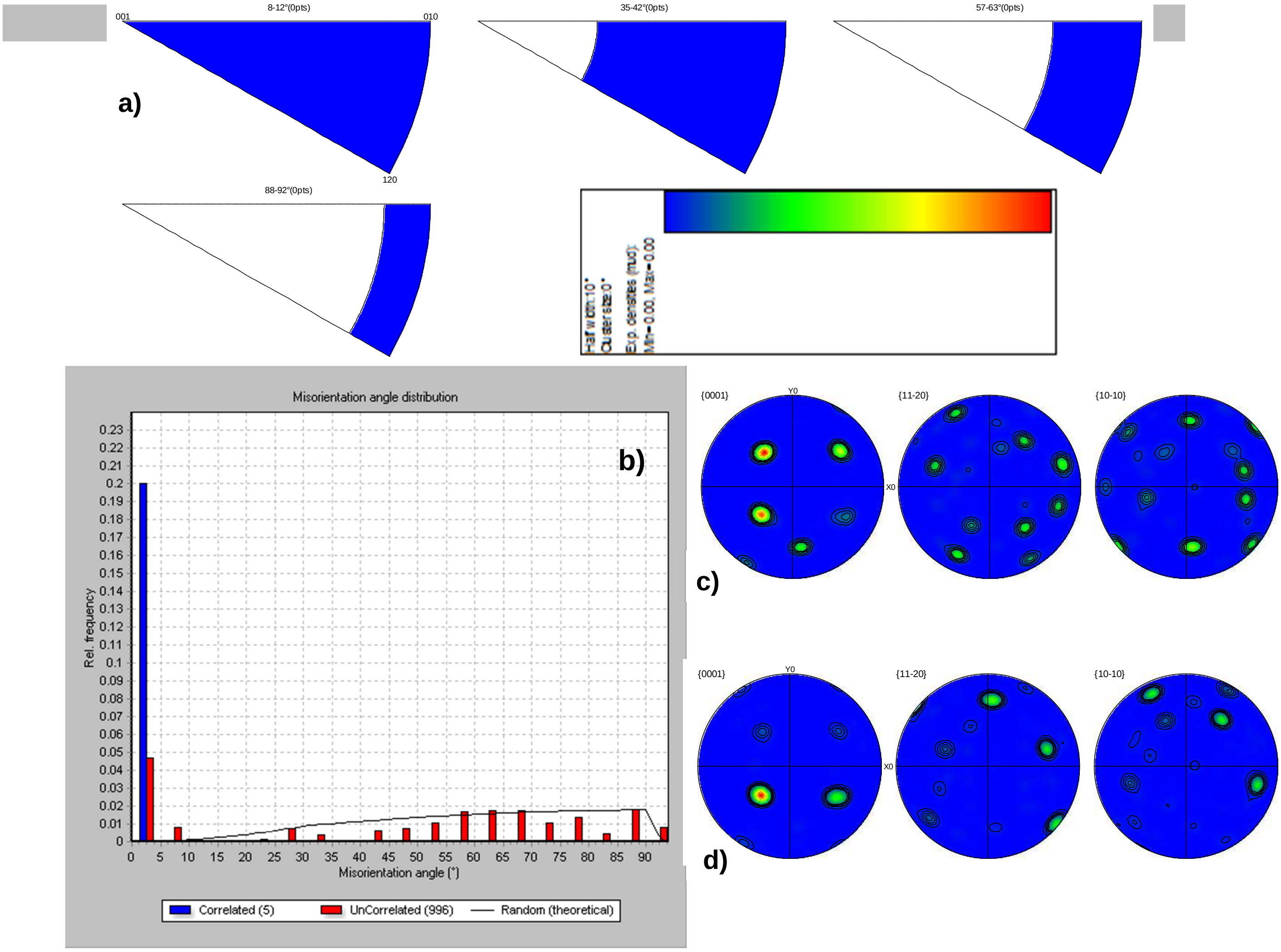

Fig.7: (a) Misorientation axes of the Ti_5Si_3 second-phase with corresponding colour coding; (b) Misorientation angle distribution (Ti_5Si_3); Pole figures of (c) α, and (d) (Ti_5Si_3)

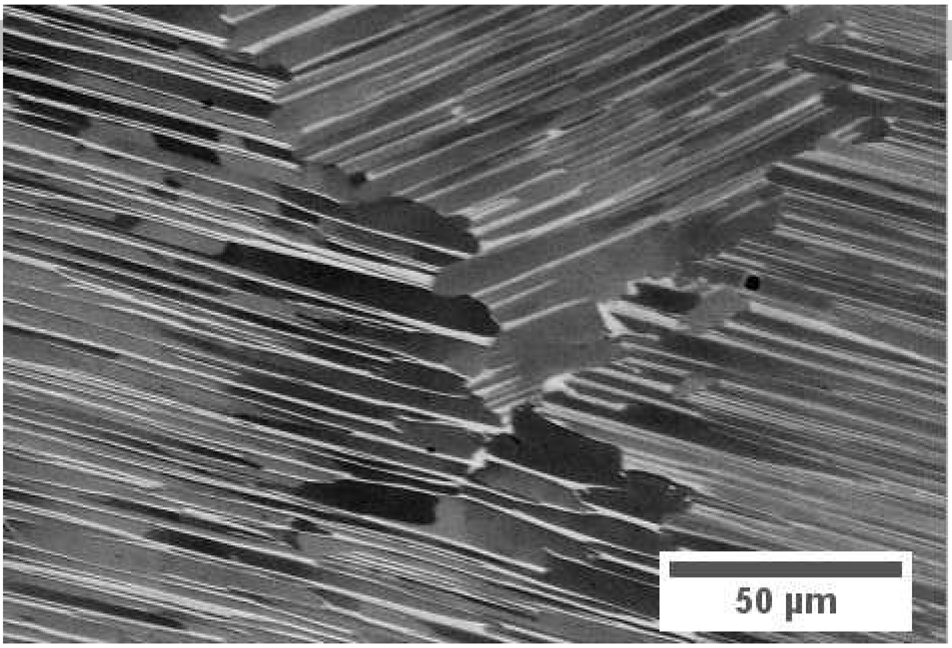

Fig.8: SEM/BSE micrograph showing a fully lamellar structure of the Ti-45Al-2Nb-0.7Cr-0.3Si

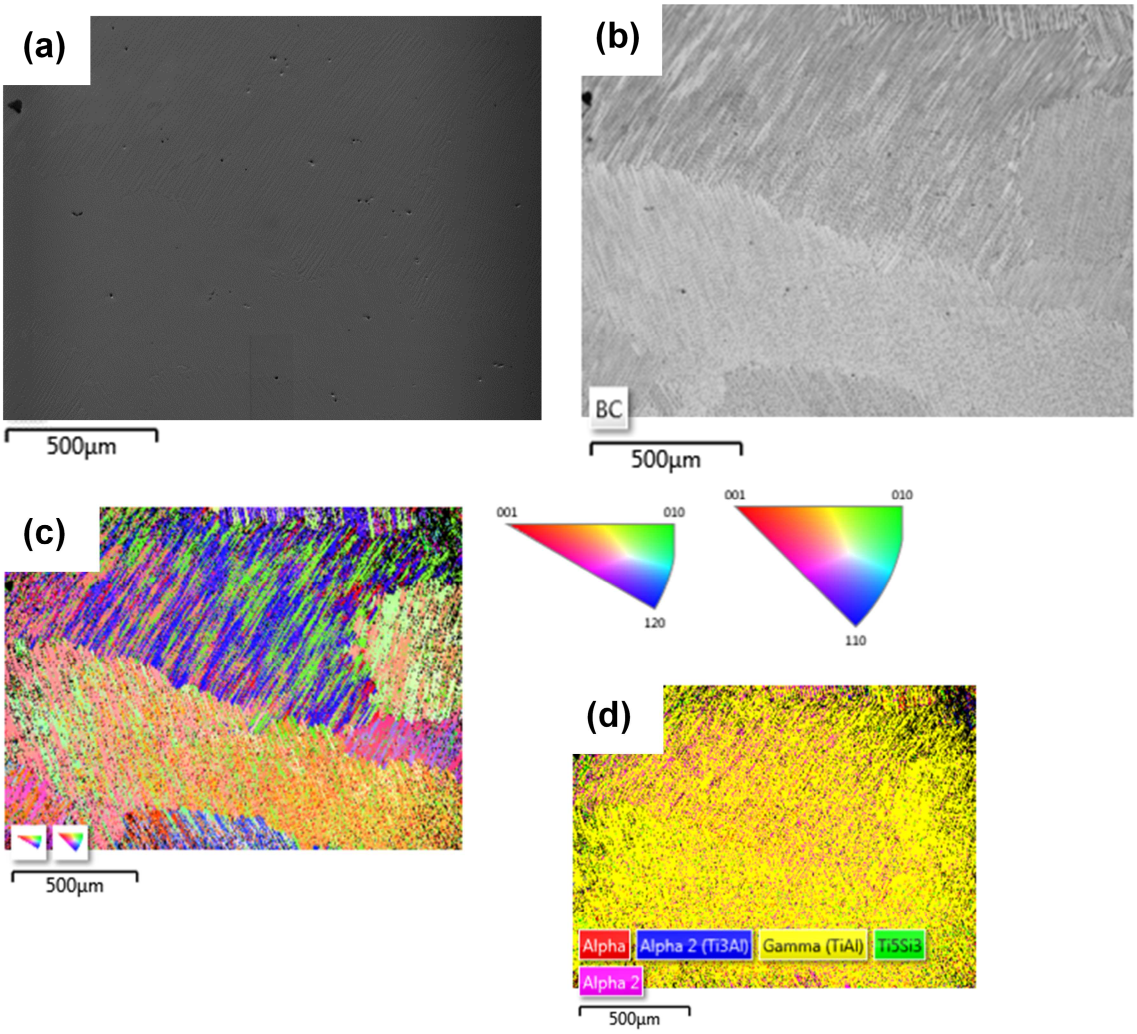

Fig.9: EBSD map of the fully lamellar Ti-45Al-2Nb-0.7Cr-0.3Si alloy: (a) Electron micrograph, (b) Band contrast image, (c) grain orientation map, and d) phase colour map.

Research Highlights

- Structure-property of γ-Ti-45Al-2Nb-0.7Cr-0.3Si intermetallic was examined.
- *ab* initio simulation package (VASP) software was used for materials design.
- Stable at room temperature in the alloy were $\gamma/\alpha_2/Ti_5Si_3$
- Formation of $\gamma/\alpha_2/Ti_5Si_3$ follows the Blackburn orientation relationship
- Ti_5Si_3/γ interface has $(011)_{\gamma} \| (0110)_{Ti5Si3}$ and $(233)_{\gamma} \| (0002)_{Ti5Si3}$.